Lawrence Berkeley National Laboratory
Energy Geosciences

Title
In Situ Continuous Monitoring of Borehole Displacements Induced by Stimulated Hydrofracture Growth

Permalink
https://escholarship.org/uc/item/8m39p599

Journal
Geophysical Research Letters, 48(4)

ISSN
0094-8276

Authors
Guglielmi, Y
Cook, P
Soom, F
et al.

Publication Date
2021-02-28

DOI
10.1029/2020gl090782

Peer reviewed

eScholarship.org Powered by the California Digital Library
University of California

In Situ Continuous Monitoring of Borehole Displacements Induced by Stimulated Hydrofracture Growth

Y. Guglielmi[1], P. Cook[1], F. Soom[1], M. Schoenball[1*], P. Dobson[1] and T. Kneafsey[1]

[1] Lawrence Berkeley National Laboratory, Energy Geosciences Division, Berkeley, CA, 94720, USA.

*Now at: Nagra, Wettingen, Switzerland

Corresponding author: (yguglielmi@lbl.gov)

Key Points:

- Hydrofracture (HF) nucleates on foliation anisotropy
- HF macroscopic propagation is in good accordance with the stress tensor and the alignment of induced seismicity
- Borehole displacements highly complement pressure data to estimate fracture orientation and growth away from the borehole

Abstract

We provide direct observations of the three-dimensional displacements of a fluid-driven fracture during water injections in a borehole at ~1.5 km depth in the crystalline rock at the Sanford Underground Research Facility (USA). Micro-shearing of the borehole initiates on a foliation plane at 61% of the minimum principal stress σ_3 . As the fluid pressure increases further up to 112% of σ_3, borehole axial and radial displacements increase with injection time highlighting the opening and sliding of a new hydrofracture growing ~10 m away from the borehole, in accordance with the ambient normal stress regime and in alignment with the microseismicity. Our study reveals how important it is to consider monitoring zonal deformation in conjunction with pressure and flow to better manage the complex hydromechanical evolution of the growing fracture.

Plain Language Summary

We provide an observation of the direct coupling between three-dimensional displacement, injection pressure and flow during growth of a hydraulic fracture in rock types (intact metamorphic rock) relevant for Enhanced Geothermal Systems and the mining industry. The displacement data indicate a complex interplay of fracture opening and fracture dilation including interaction with natural, preexisting fractures and induced seismicity.

1 Introduction

[1] Historic Enhanced Geothermal Systems (EGS) appear to show contradictory observations characterized by flow from the well mainly at preexisting fractures but at downhole fracturing pressures that exceed the minimum principal stress where hydraulic fracturing would be expected. Monitoring is usually done by reporting the borehole pressure and injected flowrate versus time, and by using passive seismic monitoring to image fracture growth (Dorbath et al., 2009; Gischig et al., 2018). These give indirect information of the fracture's extent, orientation, and an estimation of the fracture's aperture can be made by applying state-of-the-art hydraulic fracture mechanics models calibrated at the laboratory scale (Bunger and Lecampion, 2017). Microseismic clouds are often complex, both aligning into a plane perpendicular to σ_3 and showing other trends that are clearly related to faults. Field observations, mainly direct mechanical measurements in the near-field of the injection point, are thus highly incomplete. This is intrinsically challenging the successful development of enhanced geothermal projects, which strongly rely on the hydromechanical properties of the stimulated fractures that are generated to circulate water between borehole doublets (Ghassemi, 2012).

[2] Predicting how a hydrofracture initiates in the field is a challenge that depends on borehole stress concentration with respect to the in-situ stresses, fluid viscosity, injection rate, Young's modulus, fracture toughness of the rock mass, and the geometry of the borehole wall defects due to the geology and to the drilling (Jeffrey et al., 2014; Lecampion et al., 2017). After initiating, the hydrofracture may reorient from the near-borehole stress concentration region towards a direction of propagation governed by the far-field in-situ stresses and geological heterogeneities such as natural fractures (Behrmann and Elbel, 1991; Weijers et al., 1994). When the hydrofracture propagates in the far field of the borehole, the average orientation of the seismicity cloud is considered as a proxy of the fracture propagation direction (Majer and Doe, 1986). The geometrical relationship between the hydrofracture plane and the seismic event locations is not straightforward because the hydrofracture is considered propagating in mode I while mainly mode II events are observed from focal mechanisms (Zang et al., 2017). Seismicity may thus be off the fracture plane, beyond or beside the fracture propagation front and favored by stress transfer and leakage in adjacent natural fractures that are favorably oriented for shear reactivation.

[3] Here we show the direct continuous measurement of the three-dimensional displacements of an open hole section of an injection borehole during the initiation and the propagation of a hydrofracture. The hydrofracturing experiment was achieved by using a fracturing completion probe, inflating packers to

isolate a 1.6 m long zone of a 12° inclined borehole drilled parallel to σ_3 at 1478 m depth and injecting water in three successive steps separated by periods of zonal shut-in. The zone was instrumented with a strain sensor integrated into the fracturing probe and clamped on each side of a notch initially scribed to favor the creation of a fracture transverse to the borehole. The hydrofracture was propagated in 3 steps until it intersected a borehole located 10 m away from the injection hole. We show the continuous borehole displacements related to the fracture growth and we compare them with the seismicity. Using simple modeling, we estimate the fracture width and the mode of fracture growth. Finally, we discuss how these new displacement data help in assessing the role of heterogeneities and stress on improving stimulation efficiency in the development of a geothermal heat exchanger.

2 Materials and Methods

[4] The hydrofracturing experiments took place at ~1490.5 m depth in fractured metamorphic rocks of the Sanford Underground Research Facility (SURF) in South Dakota (USA, Fig. 1a and Kneafsey et al., 2019; 2020). We studied the transverse propagation of hydraulic fractures from an injection to a production subhorizontal borehole spaced about 10 m apart (respectively E1-I and E1-P in Fig. 1a). The boreholes were drilled subparallel to the local minimum principal stress σ_3 of ~21.7 MPa with an azimuth of 2 degrees and a slight plunge of 9.3 degrees to the North. The vertical stress magnitude was estimated to be ~41.8 MPa for the depth of testing. The subhorizontal intermediate principal stress σ_2 is uncertain. It was estimated to be 34.0 MPa (Wang et al., 2017; Dobson et al., 2018; Singh et al., 2019; Kneafsey et al., 2020). Six monitoring boreholes were equipped to track the fracture propagation with a wide array of sensors (Fig. 1a, Schoenball et al., 2020). Here we report on one hydrofracturing test that was set ~50 m away from the gallery in the E1-I borehole (Fig. 1a and d). The injection zone's geology is intact foliated metamorphic rock (Poorman Formation). The shallower part of the borehole displays foliation planes with a dip-azimuth/dip-angle of 35°-41°/63°-68°. The middle and lower parts are more complex with several ~0.1 m thick quartz lenses intercalated with non-planar foliation (Fig. 1d). Notches were machined in selected depth intervals of E1-I to encourage transverse fracturing upon hydraulic stimulation of these zones – this study refers to the stimulation tests conducted on the 164' (50 m) notch which, as the most representative intact rock geology of all the stimulation test intervals, was selected to initiate and propagate a fracture towards the production borehole E1-P

[5] The instrument used for isolation is a double-packer probe instrumented with a high-resolution three-dimensional displacement borehole sensor called the SIMFIP [Guglielmi et al., 2014 and Fig. 1 b-c]. The SIMFIP has a 0.2 m long and 0.1 m diameter pre-calibrated aluminum cage that is connected to two 0.25 m long elements that allow clamping both ends of the cage to the borehole wall (Fig. 1b). Cage deformations are continuously recorded with 6 optical fiber Bragg gratings (FBG) that are mechanically clamped on the 6 differently oriented wings of the cage. The fracturing zone is sealed in an open hole using the two inflatable rubber packers, which are sliding sleeves straddled by a steel mandrel (Fig. 1c). Then, the SIMFIP element is clamped to the borehole at points A and B (Fig. 1c). When it is clamped in place, the SIMFIP is independent from the straddle packer system. When the fracture initiates and propagates away from the borehole wall according to the water pressure injected in the zone, the SIMFIP directly converts the cage deformations into micrometer axial and radial borehole displacements that occur between A and B (Fig. 2 and 3). The maximum displacement range of the SIMFIP is 0.7 and 3.5 mm in the axial and radial directions of the borehole, respectively, and the accuracy is $\pm 5 \times 10^{-6}$ m. A compass set on the probe provides the orientation of measurements with 0.1° accuracy. The stimulation pressure and injected flowrate are measured simultaneously during the test.

[6] The hydraulic fracturing experiment was conducted in three steps over three days with overnight shut-in periods between each step (Fig. 2). In step 1, 2.1 liters of water was injected at a stable rate of 200 ml/min. A drop in the injection pressure occurred at 24.3 MPa. It was followed by a pressure decline to 23.2 MPa. Pressure was then increased to 26.0 MPa just before the pump was stopped, and the zone was left shut in for the night. However, a power outage caused venting of the zone pressure and of the SIMFIP

during the night. In step 2, the zone pressure was first held constant at 13.8 MPa for about 5 minutes. At the end of the step, the injected flowrate was 1.5 ml/min. Pressure was then increased to 20.7 MPa for about 1 minute, and the injected flowrate was 9 ml/min at the end of the step. The pump then maintained a pressure of 22.8 MPa but the flowrate displayed a steady increase with time indicating that the fracture created the day before during step 1 was reopening. The protocol was then switched from pressure-controlled to flowrate-controlled. The flow rate was increased in three successive steps, 0.1, 0.2 and 0.4 l/min, corresponding to injected volumes of 0.8, 0.9 and 21.8 liters, respectively (total injected volume of 23.5 liters). The pressure increased to 26.8 MPa and then decreased to a relatively constant value of 26.7 MPa just before the pump was stopped, and the zone was left shut in for the night. In step 3, a series of controlled-pressure step increments of 0.6 to 1.2 MPa was conducted up to 27.2 MPa to reopen the fracture that was propagated the day before. Reopening occurred around 20.7 to 21.7 MPa. Upon reaching 27.2 MPa, the protocol was again switched from pressure-controlled to flowrate-controlled in order to extend the fracture. The flowrate was gradually increased to a maximum value of 5 l/min until the zone was left shut in for the night. The injected volume for the third step was 80.6 liters.

[7] Acoustic image logging of the injection zone conducted after the stimulation did not show clear evidence of a new fracture, indicating that either the fracture was initiated at the notch or a preexisting foliation plane was activated during the test (Fig. 1d). Hydraulic connections between the injection zone and borehole E1-OT was detected via fiber optic temperature sensors at the end of step 2 (Schoenball et al., 2020). Step 3 hydraulic connection of the injection to the production well E1-P was directly observed with a borehole camera set in E1-P (Fig. 1a). Seismicity induced during the first step did not show any structural trend. During step 2, seismic events organized into a swarm (Fig. 4) with an average dip-azimuth/dip-angle of 159°±1.1°/83°±0.5°. The swarm grew towards the NE where it intersected E1-OT (Fig. 4, Schoenball et al., 2020). At the end of step 2, the hydrofracture extent was estimated to be a minimum of ~7-8 m given the location of E1-OT, which is 7.7 m away from the injection zone and up to 12 m based on the located seismic events (Fig. 4). During step 3, there was a much higher number of induced events because of the larger injection volume. Events aligned mainly along two new trends, one being sub-parallel to the initial one (labelled F3 in Schoenball et al., 2020) and one that finally intersected borehole E1-P at the location where the hydrofracture was found from the borehole camera observations.

3 Field data and interpretation

[8] Figure 2 shows flow and borehole radial and axial displacements versus the zone pressure during steps 1 to 3. During fracture initiation step 1, maximum displacements are about one tenth the size of those observed during the following steps of fracture growth. Initiation is characterized by borehole radial shearing (red curves) preceding axial stretching (black curves). A shear increase is observed at 12.6 MPa, which is much lower than the maximum injection pressure of 24.3 MPa. It is followed by a period of mainly axial stretching (positive axial displacement variation) until 21.5 MPa, where there is a sharp increase in shear followed by a pronounced stretching of the borehole. After the drop in injection pressure, the pressure unexpectedly increased again, generating additional borehole shearing and stretching.

[9] In steps 2 and 3, sharp variations in borehole displacements again start below the maximum injection pressure. Borehole tensile (axial) displacement initiates before shearing, which occurs at 3 to 4 MPa higher pressure. Tensile displacement starts at 18.8 and 20.4 MPa, while shearing starts at 21.5 and 23.4 MPa, respectively, in steps 2 and 3. Maximum injection pressures in steps 2 and 3 are 6 to 8 MPa higher than the onset of displacements, respectively. The pressure period of tensile displacement corresponds to the lower constant pressure steps before a significant steady increase in flowrate was observed. This reveals the hydromechanical reopening of the compliant previously created hydrofracture, which occurs before the fracture starts extending again. Shear displacements initiate at pressures where a steady increase in flowrate is observed. Borehole shearing is associated with fracture growth. Overall, both

shear and tensile displacements versus pressure increase greatly when the fracture starts extending. At the end of the shut-in periods, all steps display a significant residual shear displacement and an axial over-compression highlighting that some irreversible borehole displacement has occurred that highlights effective stress and strain changes in the borehole near field.

[10] Figure 3 shows the spatial evolution of borehole displacements. There is a significant difference in the orientation of displacements in step 1 compared to steps 2 and 3, which show comparable trends. In step 1, displacements display an initial dip-azimuth/dip-angle of 110°±10°/9°±10° up to the maximum pressure, where there is a sudden ~right angle reorientation to 035°±5°/50°±1°. The shut-in displays that same post-maximum injection pressure orientation but with a reverse sense. These displacements match well with the reactivation in shear followed by normal opening of a 224°-228°/47°-54° foliation plane affecting the zone (Fig. 3a). The shear on the plane does not induce any injection pressure variation while the opening of the plane explains the injection pressure decrease.

[11] During steps 2 and 3, an initial 020°±1°/12°±1° borehole tensile displacement might still reflect the influence of the foliation plane reopening in the borehole near-field (Fig. 3b for example). It occurs at low injection pressure. When pressure gets to 21.5 and 23.4 MPa, respectively, in steps 2 and 3, there is a reorientation of the displacements to a dip-azimuth/dip-angle of 158°±1°/40°±1°. When injection is stopped and the zone is left shut in, displacements follow a linear trend with a dip azimuth/dip angle of 334°±1°/sub-horizontal, which is the reverse of the previous trend (Fig. 3b and c). Shut-in displacement is dominated by a borehole axial contraction as observed in Figure 2 while relatively little shearing is evidenced. The shut-in displacement ends with a non-linear subhorizontal displacement sub-perpendicular to the foliation (Fig. 3a-c). This may relate to the elastic closing induced by pressure leakage in the foliation planes around the borehole. We observe that the 158°±1° displacement dip direction matches with the average 159°±1.1° plane deduced from the induced seismicity swarm and confirmed by the locations of the intersection in the monitoring borehole E1-OT (Fig. 4). The displacement dip of 40°±1° suggests a shear component on this plane during the hydrofracture growth (Fig. 3d), which is in accordance with the stress tensor orientation and the normal stress regime. This shear component is not observed during the shut-in, which corresponds to a pure normal closing of the hydrofracture (Fig. 3d). The reorientation of the displacements with injection over time shows the rotation of the hydrofracture, which initiated on a foliation defect at the borehole wall and then propagated away from the borehole near field as a new fracture plane since no such plane orientation existed prior to the test. The orientation of this new "plane" is in very good agreement with the average plane direction deduced from seismicity during step 2 (Fig. 4). Early seismicity characterized by events not aligned on the hydrofracture plane confirm that other local features at the borehole wall activated before the maximum of injection pressure occurred during step 2 (dark blue dots in Fig. 4).

4 Numerical Analysis and Discussion

[12] We used coupled hydromechanical modeling to estimate the fracture's aperture and extent from the analysis of the measured three-dimensional displacements during step 2 (supplementary material). The in-situ principal stresses inferred at the depth of the experiment (σ_1 = 41.8 MPa, σ_2 = 34 MPa, σ_3 = 21 MPa) are applied to the six boundaries of the model, and a 80 kPa/m horizontal stress gradient is set to calculate the thermomechanical stress perturbation caused by the nearby drift excavation (Fu et al., 2018). The injection is applied in a local point source in the middle of the model (E1-I in Fig. 4c). Pressure increases in a few mesh elements that are represented in an initially 0.6 m radius ruptured circular patch (Fig. S2). Outside of this circular patch, which corresponds to the fracture initiated in step 1, elements must rupture for the hydrofracture to propagate.

[13] We applied the injection protocol conducted in the field during step 2. Model results reproduce reasonably well the measured displacements and zone pressure (Figure 4). The step 1 fracture reopening is matched with fracture normal and shear stiffness values of 100 and 43 GPa/m and a plane strain Young's modulus (E') of 68.4 GPa. These values are in the range of the laboratory values obtained parallel to foliation planes affecting intact rock samples of the Poorman schist (Vigilante et al., 2017; Condon et al., 2020). During the fracture growth, some discrepancies between the model simulation and measurements relate to the strong simplification adopted in the modeling (no influence of the near borehole defects observed in step 1 was considered). At the end of the injection (at 5149 seconds in Figure 4), the calculated fracture normal opening and shear displacement are 230 and ~300 microns, respectively, at the injection point. The fracture preferentially propagated updip and downdip to a ~12 m height, and horizontally eastward to a ~7 m length, in good accordance with the size and location of the seismic swarm during step 2 (Fig. 4a and c). The fracture developed asymmetrically towards E1-OT (Fig. 4b), following the thermal stress gradient as suggested by Fu et al. (2018). Finally, the model does not reproduce the shut-in period pressure and displacement variations. In the model the switch to no-flow at the injection point maintained the pressure in the created fracture since no leakage was allowed in the surrounding block. We calculate a slight pressure drop to 23.7 MPa, which obviously is not the case in the field, where a most pronounced pressure decay is measured associated with a complete normal closing of the fracture.

[14] This fully coupled three-dimensional hydromechanical analysis shows that the displacement and seismic observations can be interpreted as a mixed-mode fracture that grows in reasonable agreement with the state of stress. We find that a 36° friction angle and a 3 MPa tensile strength of the fracture best match the observed displacement. The downward measured borehole displacement is explained by shear on the extending fracture surface (Fig. 4a-b), which develops as a complex fault given the normal stress regime. While tensile failure occurs in the fracture patch where pressure is high, shear stress builds up at the patch tip favoring shear rupture propagation (Fig. 4b). Borehole axial tension may result from the fracture hybrid opening under mode I extension and mode II shear-induced dilation. Shear rupture is one explanation for the seismic swarm, which maps the shape of the fracture surface well (Fig. 4a).

[15] The concept used in our model is that we are opening a plane that has strength and elastic properties in the range of intact rock properties parallel to foliation (Vigilante et al., 2017). The plane has no initial hydraulic conductivity. However, the orientation of the plane that was given by the alignment of the seismicity, the intersection with borehole E1-OT and the SIMFIP displacement is different from the orientation of the foliation. In addition, no such plane direction is observed among the local natural fracture families. During step 1, we observed that rupture may nucleate on foliation, eventually favored by the notch, which may have helped overcome the tensile strength. This is in good accordance with some laboratory observations showing that foliation acts as weak planes for a hydrofracture's nucleation (Jackson and Dunn, 1974; Cox and Scholz, 1988). We find that foliation creates the initiation site, but then the fracture reorients away from the well driven by stress. In our model, such a complex evolution that could eventually be related to foliation breaks normal and parallel leading to a zig-zap rupture pattern is approximated as a mixed-mode rupture along a single plane. The model is a clear oversimplification of the field case. Nevertheless, our results highlight how we can have flow concentrated at "preexisting fractures" along an EGS well, but then have microseismic and hydromechanical effects that confirm the creation of hydraulic fractures. It might be of importance in considering that the hydrofracture may extend further as a macroscale mixed-mode fault (Kamali and Ghassemi, 2018) and eventually connect to preexisting faults faster than expected, unless some leakage dissipates as part of the fluid-driven pressure into adjacent natural fractures as observed in step 3.

6 Conclusions

[16] The continuous monitoring of the transient borehole displacements associated with the initiation and propagation of an in situ hydrofracture in deep metamorphic rocks highlights the importance of mixed-mode rupture favored by shear and opening on foliation planes and a large deviatoric stress. While extending, the fracture reorientation towards ambient stress is observed at the borehole injection zone, giving a strong indication of the stress regime. The displacement response during the shut-in of the well appears as key evidence of the fracture orientation away from the borehole influence. This result is of importance because the early stimulation response appeared affected by fracture tortuosity while no clear fracture trace could be observed after the fracture stimulation. An extended test allowed best estimating both hydrofracture's properties and the state of stress because oriented strain signals from 6-to-10 meters away could be detected at the injection zone.

[17] A fracture aperture of 230 microns, height of 12 meters and length of 7 meters is deduced from the analysis of borehole displacements. This is in good agreement with the size of the seismic swarm and other data showing evidence of the fracture intersecting neighboring boreholes. These fracture dimensions are explained by the additional shear stress concentration at the fracture tip, which may enhance fracture growth when its size is large enough to behave as a macroscale fault. Thus, even a small injected volume can create a large fracture at depth in hard rocks, contributing to the risk to connect to preexisting faults and to trigger larger than expected earthquakes. Adding displacement measurements in the deep borehole stimulation zone allows for better control of the real-time growth of a hydrofracture, by tracking if the growth develops along a preexisting defect with associated slip or if it is oriented given the full stress tensor's characteristics.

Acknowledgments, Samples, and Data

This material was based upon work supported by the U.S. Department of Energy, Office of Energy Efficiency and Renewable Energy (EERE), Office of Technology Development, Geothermal Technologies Office, under Award Number DE-AC02-05CH11231 with LBNL. This work is one of the contributions of the EGS Collab Team. The research supporting this work took place in whole or in part at the Sanford Underground Research Facility in Lead, South Dakota. The assistance of the Sanford Underground Research Facility and its personnel in providing physical access and general logistical and technical support is acknowledged. Data access is provided under the common Enabling FAIR data Project guidelines at the U.S. Department of Energy Geothermal Data Repository (https://gdr.openei.org/submissions/1250).

References

Behrmann, L. A., and J. L. Elbel. Effect of perforations on fracture initiation. *Journal of Petroleum Technology* **43(5)**, 608–615. SPE 20661, 1991.

Berčáková, A., R. Melichar, Y. Obara, J. Ptáček, and K. Souček. Evaluation of Anisotropy of Fracture Toughness in Brittle Rock, Migmatized Gneiss. *Procedia Engineering*, **191**, 900–907, 2017.

Bunger, A. P. and B. Lecampion. Four critical issues for successful hydraulic fracturing applications. *In X.-T. Feng, editor, Rock Mechanics and Engineering, Volume 5 (Surface and Underground Projects)*, Chapter 16. CRC Press/Balkema, 2017.

Chai, C., Maceira, M., Santos-Villalobos, H., Venkatakrishnan, S. V., Schoenball, M., Zhu, W., et al.. Using a Deep Neural Network and Transfer Learning to Bridge Scales for Seismic Phase Picking. *Earth and Space Science Open Archive*. https://doi.org/10.1002/essoar.10503021.1, 2020.

Condon, K., H. Sone, H. F. Wang, and EGS Collab Team. Low Static Shear Modulus Along Foliation and Its Influence on the Elastic and Strength Anisotropy of Poorman Schist Rocks, Homestake Mine, South Dakota. *Rock Mechanics and Rock Engineering*, 2020.

Cox, S. J. D., and C. H. Scholz. On the formation and growth of faults: an experimental study. *Journal of Structural Geology*, **10 (4)**, 413–430, 1988.

Detournay, E., and E. Carbonell. Fracture mechanics analysis of the breakdown process in minifracture or leakoff test. SPE paper 28076, *Soc. Pet. Eng. Prod. Facil.*, **12**, 195–199, 1997.

Detournay, E. Hydraulic Conductivity of Closed Rock Fracture: an Experimental and Analytical Study, in *Proceedings of the 13th Canadian Rock Mechanics Symposium*, 168–173, 1980.

Dobson, P., T. Kneafsey, J. Morris, A. Singh, M. Zoback, W. Roggenthen, T. Doe, G. Neupane, R. Podgorney, H. Wang, H. Knox, P. Schwering, D. Blankenship, C. Ulrich, T. Johnson, M. White, and the EGS Collab team. The EGS Collab hydroshear experiment at the Sanford Underground Research Facility – Siting criteria and evaluation of candidate sites. *Geothermal Resources Council Transactions*, **42**, 708–723, 2018.

Dorbath, L., N. Cuenot, A. Genter, and M. Frogneux. Seismic response of the fractured and faulted granite of Soultz-sous-Forets (France) to 5 km deep massive water injections. *Geophysical Journal International*, **177(2)**, 653–675, doi:10.1111/j.1365-246X.2009.04030.x, 2009.

Fu, P., M. White, J. Morris, T. Kneafsey, and E. C. Team. Predicting Hydraulic Fracture Trajectory Under the Influence of a Mine Drift in EGS Collab Experiment I, in *Proceedings of the 43rd Workshop on Geothermal Reservoir Engineering*, Stanford University, Stanford, California, 2018.

Ghassemi, A. A Review of Some Rock Mechanics Issues in Geothermal Reservoir Development. *Geotech Geol Eng*, **30**, 647–664, doi:10.1007/s10706-012-9508-3, 2012.

Gischig, J., J., Doetsch, H., Maurer, H. Krietsch, F. Amann, K. F. Evans, M. Nejati, M. Jalali, B. Valley, A. C. Obermann, S. Wiemer, and D. Giardini. On the link between stress field and small-scale hydraulic fracture growth in anisotropic rock derived from microseismicity. *Solid Earth*, **9**, 39–61, 2018.

Guglielmi, Y., F. Cappa, H. Lançon, J. B. Janowcsyk, J. Rutqvist, C.-F. Tsang, and J. S. Y. Wang. ISRM Suggested Method for Step-Rate Injection Method for Fracture In-Situ Properties (SIMFIP): Using a 3-Components Borehole Deformation Sensor. *Rock Mechanics and Rock Engineering*, **47(1)**, 303–311. doi:10.1007/s00603-013-0517-1, 2014.

Guglielmi, Y., F. Cappa, J.-P. Avouac, P. Henry, and D. Elsworth. Seismicity triggered by fluid injection-induced aseismic slip. *Science*, **348(6240)**, 1224–1226, DOI: 10.1126/science.aab0476, 2015.

Itasca Consulting Group. 3DEC, 3-Dimensional Distinct Element Code. Itasca Consulting Group, Minneapolis, MN, 2016.

Jackson, R. E., and D. E. Dunn. Experimental Sliding Friction and Cataclasis of Foliated Rocks. *Int. J. Rock Mech. Min. Sci. & Geomech. Abstr.*, **11**, 235–249, 1974.

Jeffrey, R. G., Z. R. Chen, X. Zhang, A. P. Bunger, and K. W. Mills. Measurement and analysis of full-scale hydraulic fracture initiation and fracture reorientation. *Proceeding of the 48th US Rock Mechanics / Geomechanics Symposium*, Minneapolis, USA, 2014.

Kamali, A. and A. Ghassemi. Analysis of injection-induced shear slip and fracture propagation in geothermal reservoir stimulation. *Geothermics*, **76**, 93–105, 2018.

Kneafsey, T. J., D. Blankenship, H. A. Knox, T. C. Johnson, J. B. Ajo-Franklin, P. C. Schwering, P. F. Dobson, J. P. Morris, M. D. White, P. Fu., R. Podgorney, L. Huang, B. Johnston, W. Roggenthen, T. Doe, E. Mattson, A. Ghassemi, C. Valladao, and the EGS Collab team. EGS Collab Project: Status and Progress. In *Proceedings of the 44th Workshop on Geothermal Reservoir Engineering*, Stanford University, 16 p., 2019.

Kneafsey, T. J., D. Blankenship, P. F. Dobson, J. P. Morris, M. D. White, P. Fu, P. C. Schwering, J. B. Ajo-Franklin, L. Huang, M. Schoenball, T. C. Johnson, H. A. Knox, G. Neupane, J. Weers, R. Horne, Y. Zhang, W. Roggenthen, T. Doe, E. Mattson, C. Valladao, and the EGS Collab team. The EGS Collab project: Learnings from Experiment 1. *Proceedings, 45th Workshop on Geothermal Reservoir Engineering*, Stanford University, 15 p., 2020.

Lecampion, B., J. Desroches, R. G. Jeffrey, and A. P. Bunger. Experiments versus theory for the initiation and propagation of radial hydraulic fractures in low-permeability materials. *J. Geophysical Res. Solid Earth*, **122**, 1239–1263, doi:10.1002/2016JB013183, 2017.

Majer, E. and T. Doe. Studying hydrofractures by high frequency seismic monitoring, *Int. J. Rock Mech. Min.*, **23**, 185–199, https://doi.org/10.1016/0148-9062(86)90965-4, 1986.

Oak Ridge National Laboratory. (2020). EGS Collab Experiment 1: 3D Seismic Velocity Model and Updated Microseismic Catalog Using Transfer-Learning Aided Double-Difference Tomography [data set]. Retrieved from https://dx.doi.org/10.15121/1632061.

Schoenball, M., J. B. Ajo-Franklin, D. Blankenship, C. Chai, A. Chakravarty, P. Dobson, C. Hopp, T. Kneafsey, H. A. Knox, M. Maceira, M. C. Robertson, P. Sprinkle, C. Strickland, D. Templeton, P. C. Schwering, C. Ulrich, T. Wood and the EGS Collab Team. Creation of a mixed-mode fracture network at meso-scale through hydraulic fracturing and shear stimulation. *J. Geophys. Res. Solid Earth*, doi: 10.1029/2020JB019807. 2020.

Singh, A., M. Zoback, P. F. Dobson, T. J. Kneafsey, M. Schoenball, Y. Guglielmi, C. Ulrich, W. Roggenthen, N. Uzunlar, J. Morris, P. Fu, P. C. Schwering, H. A. Knox, L. Frash, T.W. Doe, H. Wang, K. Condon, B. Johnston and the EGS Collab team. Slip tendency analysis of fracture networks to determine suitability of candidate testbeds for the EGS Collab hydroshear experiment. *Geothermal Resources Council Transactions*, **43**, 405–424, 2019.

Stoeckhert, F., S. Brenne, M. Molenda, and M. Alber. Mode I fracture toughness of rock under confining pressure. *Rock Mechanics and Rock Engineering: From the Past to the Future – Ulusay et al. (Eds), Taylor & Francis Group, London*, ISBN 978-1-138-03265-1, 2016.

Vigilante, P. J., H. Sone, H. F. Wang, B. Haimson, and T. W. Doe. Anisotropic Strength of Poorman Formation Rocks, kISMET Project. *51st US Rock Mechanics / Geomechanics Symposium, San Francisco, California USA, 25-28 June 2017*, ARMA 17-766, 2017.

Wang, H. F., M. Y. Lee, T. Doe, B. C. Haimson, C. M. Oldenburg, and P. F. Dobson. In-situ stress measurement at 1550-meters depth at the kISMET test site in Lead, S.D. *In 51st US Rock Mechanics / Geomechanics Symposium*. San Franscisco, California, USA: American Rock Mechanics Association, ARMA 2017–0651, 7 p., 2017.

Weijers, L., C. J. de Pater, K. Owens, and H. Kogsbøll. Geometry of hydraulic fractures induced from horizontal wellbores. *SPE Production & Facilities*, **9(2)**, 87–92, SPE 25049, 1994.

Witherspoon, P. A., J. S. Y. Wang, K. Iwai, and J. E. Gale. Validity of cubic law for fluid flow in a deformable rock fracture, *Water Resour. Res.*, **16(6)**, 1016–1024, 1980.

Zang, A., O. Stephansson, L. Stenberg, K. Plenkers, S. Specht, C. Milkereit, E. Schill, G. Kwiatek, G. Dresen, G. Zimmermann, T. Dahm, and M. Weber. Hydraulic fracture monitoring in hard rock at 410 m depth with an advanced fluid-injection protocol and extensive sensor array. *Geophysical Journal International*, **208(2)**, 790–813, doi:10.1093/gji/ggw430, 2017.

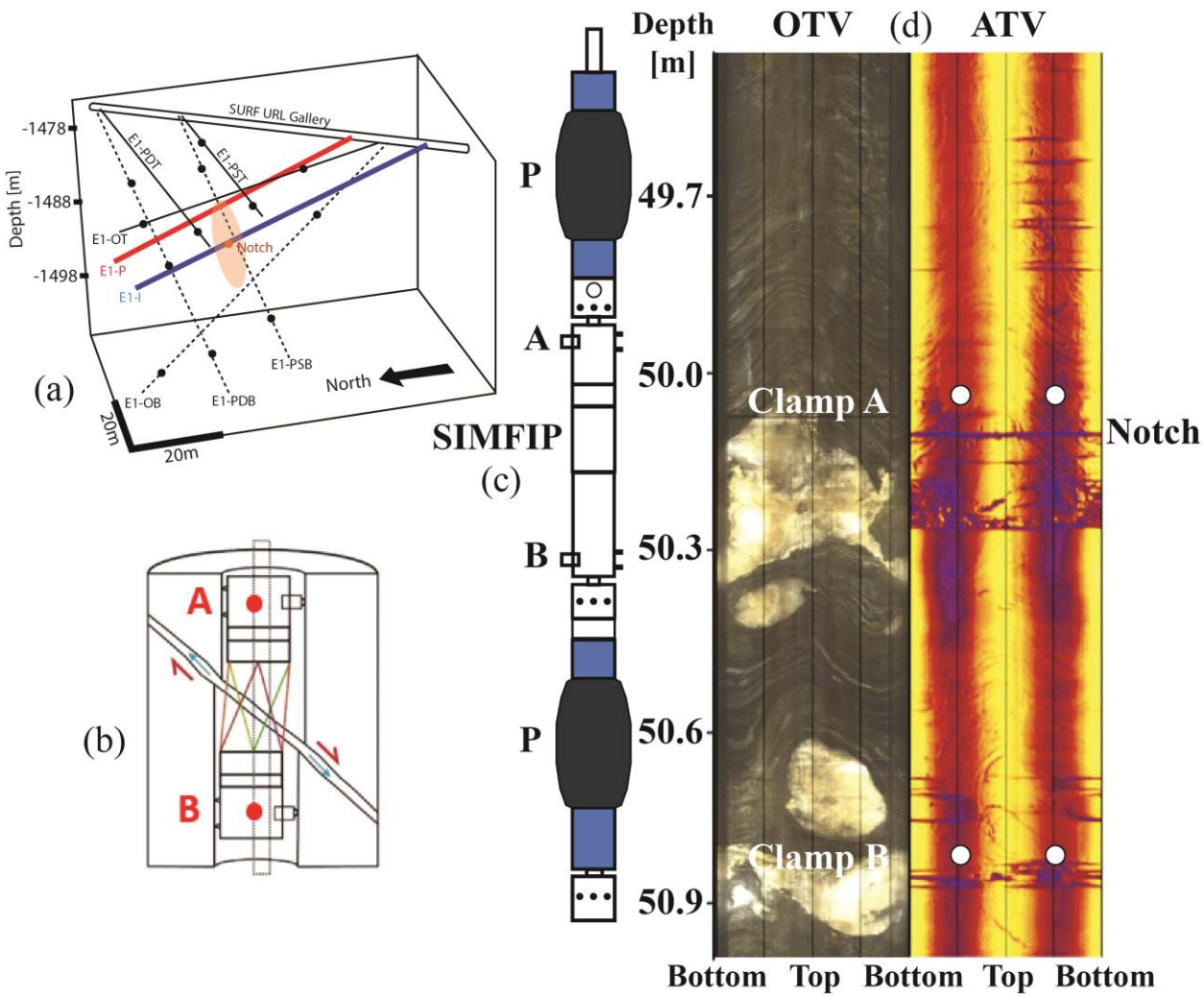

Figure 1: Experiment setting - (a) stimulated volume at ~1500m depth below ground surface – the injection borehole is depicted in blue (E1-I), and the production borehole in red (E1-P); (b) – SIMFIP instrument measuring the relative displacement between two points A and B clamped across an activated borehole fracture. (c) – Borehole hydrofracturing probe with the two inflatable packers (P), the clamping points A and B and the SIMFIP instrument. (d) - Optical (OTV) and acoustic (ATV) images of the stimulated intervals. Quartz lenses are white zones in the OTV image. Foliation planes are light and dark grey sigmoids above 50m. Below 50m, the quartz lenses deform the sigmoids. The ATV image mainly highlights horizontal stripes that were all generated by the notching tool. Most of them are minor carvings of the borehole wall.

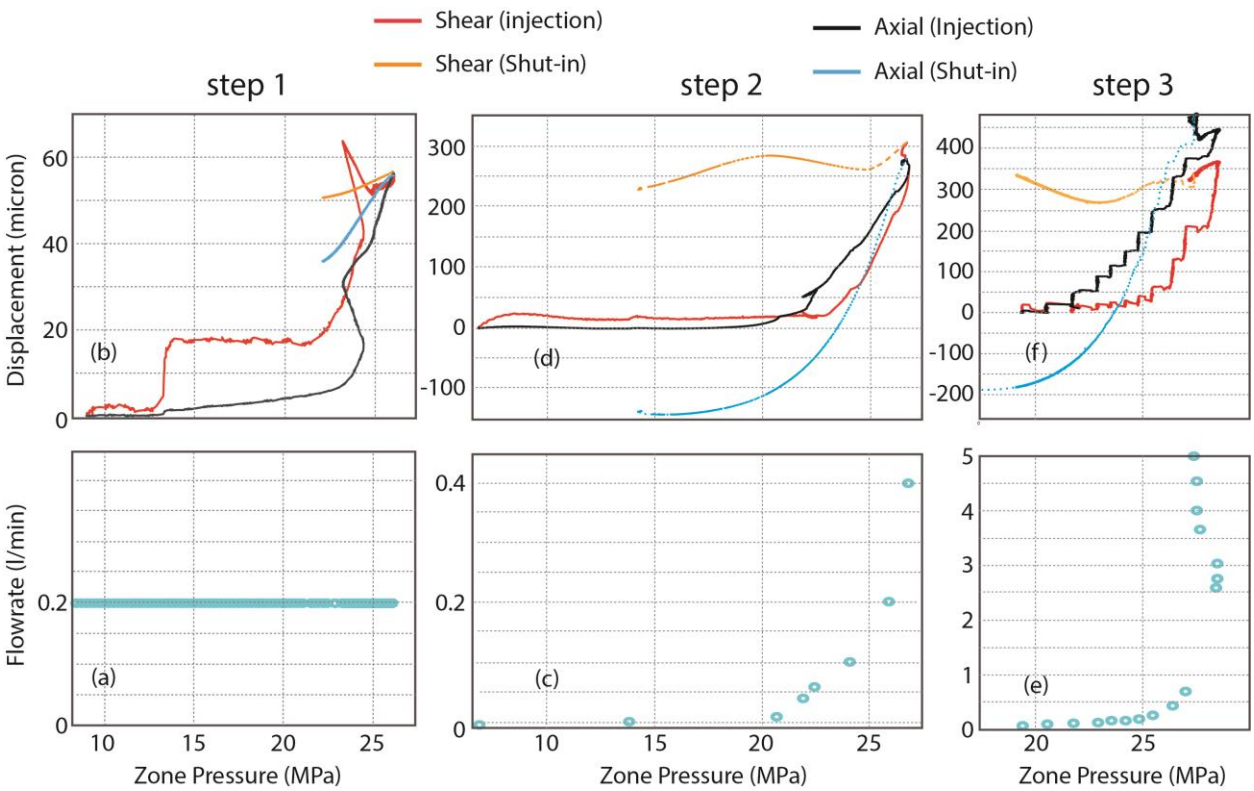

Figure 2: Displacements in borehole coordinates and flowrate variations versus pressure. Upper row shows the borehole displacement variations versus the injection pressure. Lower row shows the injected flowrate variation versus the injection pressure.

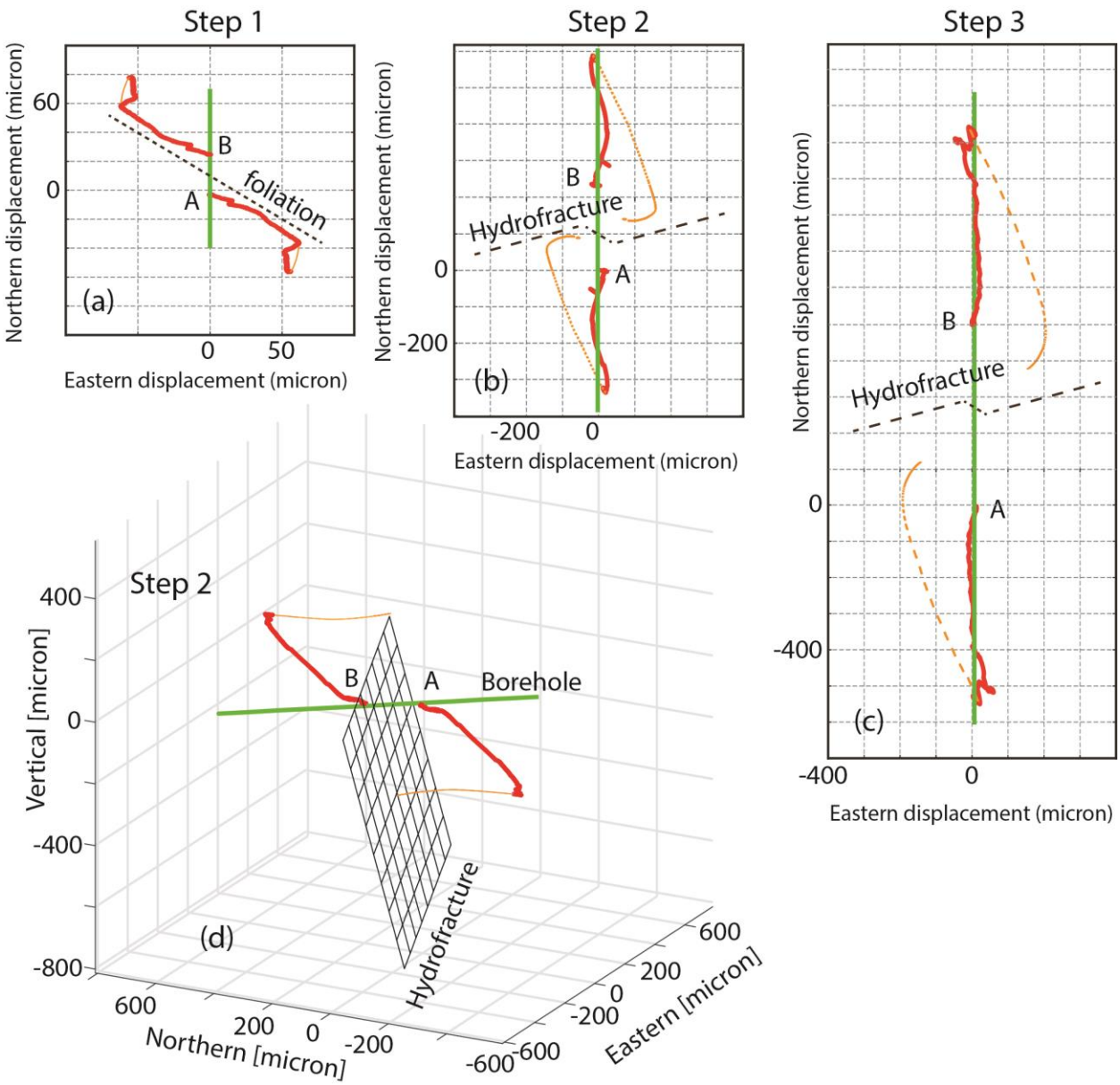

Figure 3: Borehole displacement (in geographic coordinates) evolution during stimulation. Map view of (a) step 1, (b) step 2 and (c) step 3 displacements. (d) Displacement evolution during step 2. Red curve is the displacement during the injection. Orange curve is the displacement during the shut-in. The green line depicts the orientation of the borehole. In all the figures, the distance between A and B is not to scale.

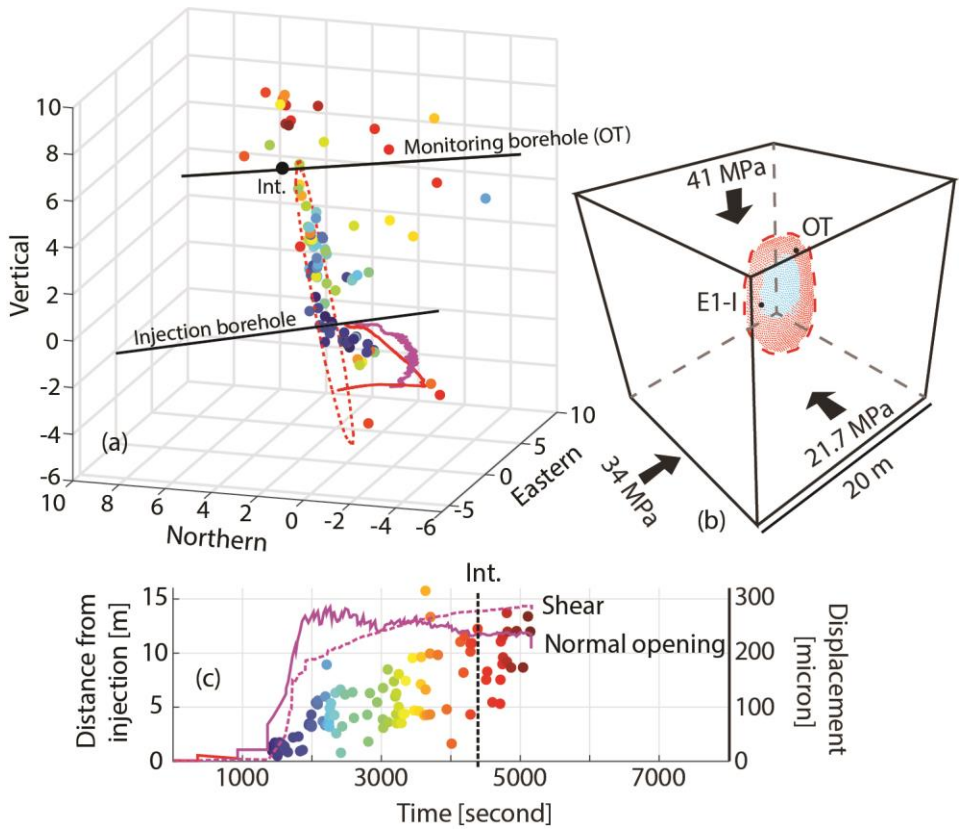

Figure 4: Model results of step 2 hydrofracture propagation. (a) Three dimensional view of the injection borehole E1-I and monitoring hole E1-OT, which was intersected by the hydraulic fracture at point *Int*. Circles are the localized induced seismic events color coded by their time of occurrence (see plot (c) for actual color mapping of times) during stimulation step 2 (location of events is taken from Oak Ridge National Laboratory, 2020 and Chai et al., 2020). The red dashed circle line is the extent of the calculated hydrofracture in Fig. 4b. The red continuous curve shows the displacement measured at the injection borehole while the magenta curve shows the modeled displacement. (b) Numerical model setting with the calculated fracture at the end of the injection. Blue circles depict tensile failure and red circles depict shear failure. (c) Normal and shear displacement of the hydrofracture at the injection point E1-I compared to the spatio-temporal evolution of seismicity.